

CrossMark
click for updates

Research

Cite this article: Wan H, Dong H, Gai K. 2015Computational investigation of cicada aerodynamics in forward flight. *J. R. Soc. Interface* **12**: 20141116.<http://dx.doi.org/10.1098/rsif.2014.1116>

Received: 9 October 2014

Accepted: 10 November 2014

Subject Areas:

biomechanics, biomimetics, biophysics

Keywords:

insect free flight, insect aerodynamics, low Reynolds number flow

Authors for correspondence:

Hui Wan

e-mail: hui.wan.ctr@wpafb.af.mil

Haibo Dong

e-mail: haibo.dong@virginia.eduElectronic supplementary material is available at <http://dx.doi.org/10.1098/rsif.2014.1116> or via <http://rsif.royalsocietypublishing.org>.

Computational investigation of cicada aerodynamics in forward flight

Hui Wan¹, Haibo Dong² and Kuo Gai³¹Aerospace Systems Directorate, Air Force Research Laboratory, WPAFB, OH 45433, USA²Department of Mechanical and Aerospace Engineering, University of Virginia, Charlottesville, VA 22904, USA³Department of Mechanical and Materials Engineering, Wright State University, Dayton, OH 45435, USA

Free forward flight of cicadas is investigated through high-speed photogrammetry, three-dimensional surface reconstruction and computational fluid dynamics simulations. We report two new vortices generated by the cicada's wide body. One is the thorax-generated vortex, which helps the downwash flow, indicating a new phenomenon of lift enhancement. Another is the cicada posterior body vortex, which entangles with the vortex ring composed of wing tip, trailing edge and wing root vortices. Some other vortex features include: independently developed left- and right-hand side leading edge vortex (LEV), dual-core LEV structure at the mid-wing region and near-wake two-vortex-ring structure. In the cicada forward flight, approximately 79% of the total lift is generated during the downstroke. Cicada wings experience drag in the downstroke, and generate thrust during the upstroke. Energetics study shows that the cicada in free forward flight consumes much more power in the downstroke than in the upstroke, to provide enough lift to support the weight and to overcome drag to move forward.

1. Introduction

The aerodynamics of insects' flight has been extensively studied both experimentally and numerically, towards answering the central question of how lift is augmented by unsteady wing motion [1]. Many aerodynamic mechanisms of force generation by flapping wings have been proposed based upon studies on rigid mechanical models, including wing-wake interactions and rotational circulation [2], delayed stall during the translation portion of the stroke [3], axial flow stabilized leading edge vortex (LEV) [4] and rotational accelerations [5]. Although studies on wing models have substantially advanced the understanding of insects' flight, the wing model has intrinsic restrictions such as wing rigidity and simplified kinematics. Tethered real insects were therefore studied to investigate the leading edge vortices [6], the flow [7] and the vortex structures in the wake [8–10]. For example, the stereophotographs of flow past tethered tobacco hawkmoths (*Manduca sexta*) showed the alternating horizontal and vertical vortex rings in the wake structure [11]. Quantitative measurements of flow field in the LEV of *M. sexta* showed that the LEV was continuous across the thorax and runs to each wingtip [6]. Although flow visualizations on free and tethered dragonflies have shown some similar properties [12], the tethered flights can nevertheless convincingly reproduce the scenarios of free flight [13], in both kinematics [14] and force generation [15]. Hence, studies on the aerodynamics of insects in free flight are consistently pursued [16–24]. It has been pointed out that insects generate forces through a quite complex combination of aerodynamic mechanisms, including wake capture, active and inactive upstrokes, clap and fling, and LEV. The involved mechanisms may even vary in successive strokes [16].

One factor ignored in most studies of insects' free flight is the insect body. With no intention of comparing the body morphology of various insects, we here roughly characterize insects with slender or wide bodies using the non-dimensional mean body diameter (\hat{d}) defined as $\hat{d} = (4M/\pi\rho_b l_b^3)^{1/2}$ [25]. M and l_b are the mass and the body length, respectively. The body density ρ_b is 1.1 mg mm^{-3} . The above \hat{d} is basically defined as the body width-to-length ratio. Some insects with various body widths are shown in table 1, from which we can see that dragonflies have

Table 1. Non-dimensional body width of several insects.

insects	l_b (mm)	l_b/l	M (mg)	d (mm)	b (mm)	d/b	\hat{d}
dragonfly [26]	70.5	1.413	790	3.60	101.8	0.0354	0.0511
	72	1.361	790	3.56	105.8	0.0337	0.0495
hawkmoth, M1 [19]	42.49	0.876	1579	6.54	103.5	0.0632	0.154
hawkmoth, F2 [19]	42.57	0.817	1995	7.36	111.6	0.0660	0.173
bumblebee, worker 01 [25]	18.6	1.41	175	3.35	34.2	0.0978	0.180
bumblebee, queen 03 [25]	21.3	1.45	595	5.32	42.3	0.126	0.250
beetles, B4 [23]	—	—	6800	18	160	0.112	—
beetles, B6 [23]	—	—	6900	10	148	0.0676	—
cicada (this paper)	30.2	0.857	1181	6.75	84.7	0.0797	0.225

slender bodies, with \hat{d} around 0.05. Body widths of hawkmoths and bumblebee workers are in an intermediate range of 0.15–0.18. The cicada and the queen bumblebee both possess wide bodies, with \hat{d} above 0.2. Using \hat{d} as defined above is actually an underestimation of the cicada body width, because the cross section of the cicada body is close to an oval shape, with the major axis aligning with the body width direction. Despite this underestimation, the cicada body is still shown to be wide in table 1. The body-length-to-wing-length ratio, l_b/l , is also calculated in table 1, showing that the cicada has a short body length among the insects listed. It is noteworthy that body width (d) can also be categorized by other parameters such as the ratio of the body width to the wing span (b), i.e. d/b , as shown in table 1. The ratio \hat{d} of the beetles [23] was not calculated owing to the lack of body length data. The body width d was obtained from the subtraction of wing length from wing span. It is interesting to note that the ratio d/b varies quite a bit for beetles with comparable body mass. From both the ratio d/b and the ratio of body width to length (\hat{d}), it is reasonable to consider the cicada in this study as one having a wide body.

The flight mechanism of insects with a wide body such as cicada may inspire the biomimetic design of flapping wing-based micro air vehicles [27] to carry large payloads. In this study, a high-speed photogrammetry system and three-dimensional surface reconstruction technology are used to reveal cicada wing kinematics during a free forward flight. The aerodynamic performance is then studied using an in-house immersed-boundary-method-based computational fluid dynamics (CFD) solver. To the best of our best knowledge, this is the first study on the three-dimensional vortex formation and unsteady aerodynamics in free-flying cicadas.

2. Material and methods

2.1. Cicada (*Tibicen linnei*) morphology and surface reconstruction

Cicadas selected in this study are of the *Tibicen* genus, which is the most common species in the Dayton area of Ohio, USA. The wings of a cicada are folded back and aligned along its body when at rest. During flight, the hindwing of the cicada is hooked with the forewing by a grooved coupling along the hindwing costa and the forewing margin [28]. The coupled forewing and hindwing perform like one wing composed of two pieces, with a certain deflection angle in between. It is also interesting to note that bumblebees hook their forewings and hindwings in a similar manner

Table 2. Morphological data for the cicada in this study.

variable	value
body mass (mg)	1181 \pm 0.5
body length (mm)	30.2 \pm 0.05
forewing/hindwing length (mm)	35.0/19.9 \pm 0.05
forewing/hindwing chord at mid-wing (mm)	9.3/9.6 \pm 0.05
forewing planform area (mm ²)	326 \pm 2
hindwing planform area (mm ²)	165 \pm 5
wing span (mm)	84.7 \pm 0.05
wing load (N m ⁻²)	11.8 \pm 0.2
flapping frequency (Hz)	47 \pm 1

[21]. In the flow simulation we conducted, the forewing and hindwing are actually combined and treated as one wing for ease of numerical simulation. The morphology of the cicada wings is measured when they spread out as in mid-downstroke, using techniques similar to the measurement of hummingbirds [29]. The obtained morphological data are listed in table 2.

The cicada flight was filmed in a large room, without any constraint from tethering or wind tunnel walls. The room temperature was around 27°C, and the air in the room was assumed to be quiescent. The photogrammetry set-up consists of three synchronized Photron FASTCAM SA3 60 K high-speed cameras (with 1024 \times 1024 pixel resolution), which were aligned orthogonal to each other and were operated at 1000 fps. Cicadas were illuminated by three halogen photo-optic lamps (OSRAM, 54428).

The cicada flight is reconstructed using a template-based hierarchical subdivision surface method. The details about this method and its accuracy can be found in [30]. For completeness, we briefly summarize it here using one wing as an example. Before the videotaping, the cicada wing was marked in a grid pattern with black ink marker points to facilitate the three-dimensional surface reconstruction. After the videotaping was done, an initial wing template was generated with Catmull–Clark subdivision surfaces [31] by aligning the first-level surface points with the marker points. Catmull–Clark subdivision surface is a specific cubic spline surface representation that can generate smooth surfaces from meshes of arbitrary topology [32]. Once the initial wing template surface has been created, marker points are digitized in each recorded image at each time step. The vertices on the smooth wing template surfaces corresponding to the first level of the subdivision surface hierarchy are then iteratively aligned to the three-dimensional projections of each marker point, until

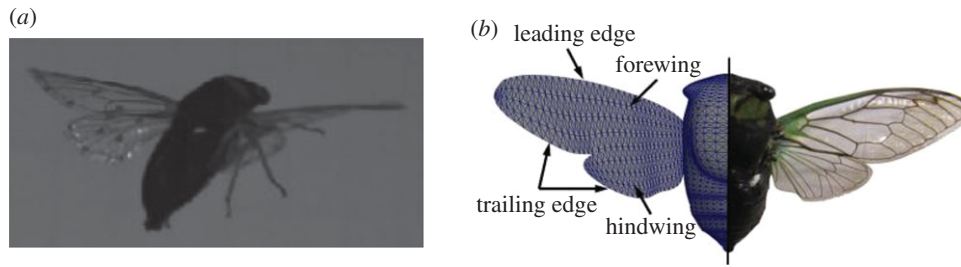


Figure 1. Real cicada and its reconstruction. (a) Raw picture and (b) comparison of real and reconstructed cicada. (Online version in colour.)

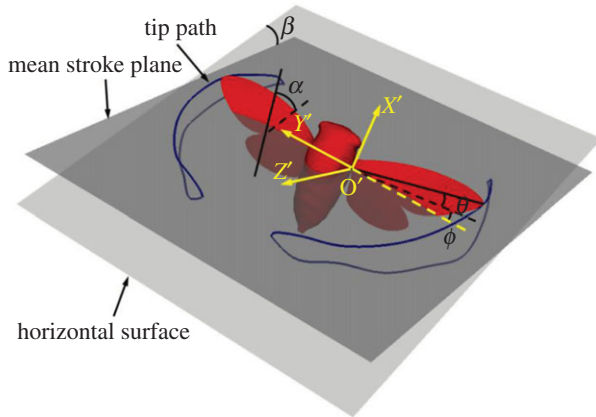


Figure 2. Polar coordinates defined by three Euler angles; the wing position shown here is at the mid-downstroke. (Online version in colour.)

further iterations produce no additional change in the reconstructed wing surface. As an example, figure 1*a* shows a raw picture of a cicada during downstroke. Figure 1*b* presents a comparison between a real cicada and the reconstructed result.

2.2. Cicada wing kinematics

Figure 2 shows the three Euler angles defining the wing position in the wing-root coordinate system ($X'Y'Z'$), in which the X' -axis is parallel with the body longitudinal direction, the Y' -axis is along the lateral direction and the Z' -axis complies with the right-hand rule. The mean stroke plane connected the wing root and wingtips at the start and end of the downstroke. The stroke position angle $\phi(t)$ defines the angular position of the wing in the mean stroke plane, with 0° aligning with the negative direction of the Y' -axis. The deviation angle $\theta(t)$ is the angle between the base-to-wingtip line and the mean stroke plane. The pitch angle $\alpha(t)$ is defined as the angle of the wing chord with respect to the tangent of the wing trajectory.

2.3. Computational fluid dynamics simulation

Advanced CFD methodologies have been proposed to address fluid dynamics of moving objects, such as the immersed-boundary method [33,34] and the overset grid method [35]. In this study, we used a well-validated in-house CFD solver simulating incompressible flow past three-dimensional moving bodies. The incompressible flow is governed by the Navier–Stokes equations

$$\nabla \cdot \mathbf{u} = 0; \quad \frac{\partial \mathbf{u}}{\partial t} + \mathbf{u} \cdot \nabla \mathbf{u} = -\frac{1}{\rho} \nabla p + \nu \nabla^2 \mathbf{u}, \quad (2.1)$$

where \mathbf{u} is the velocity vector in the Cartesian coordinate system, t is time and p is the pressure. The fluid density and kinematic viscosity are denoted by ρ and ν , respectively. The Navier–Stokes equations (2.1) are integrated in time using a fractional step method. Second-order central difference schemes in space

are employed to both convection and diffusion terms. One validation case using the CFD solver is shown in appendix A. More details on the numerical algorithm and immersed-boundary treatment, as well as validations, can also be found in previous publications [34].

In this study, a Cartesian grid of size $265 \times 149 \times 249$ (about 9.2 million) is used for the whole computational domain ($30\bar{c} \times 30\bar{c} \times 30\bar{c}$), wherein a region of $7.5\bar{c} \times 4\bar{c} \times 7\bar{c}$ is located in the domain centre with uniform fine grids ($\Delta \cong 0.032$). The stretching grids are applied in all three directions from the fine region to the outside boundaries. Grids around the wing and the cicada body are shown in the electronic supplementary material, figure S1. The time step (Δt) in this study is 0.001 to ensure stable solutions obtained throughout the simulation. The outside boundary conditions of both velocity and pressure are homogeneous Neumann conditions. The inner boundary composed by the cicada body and wings is prescribed according to the surface reconstruction results.

The Reynolds number is defined by $Re = \bar{c} U_{ref}/\nu$, where the kinematic viscosity ν is around $1.56 \times 10^{-5} \text{ m}^2 \text{ s}^{-1}$ for air at room temperature (27°C), and \bar{c} is the mean chord length (14.0 mm) from the leading edge of the forewing to the trailing edge of the hindwing, because the cicada forewing and hindwing are hooked together during flight. The average speed of forward flight, the reference velocity U_{ref} , is measured as 2.21 m s^{-1} . The reduced frequency is defined as $k = fl/U_{ref}$, where f is the flapping frequency, and l is the length of the forewing from the wing root to the wingtip, with the value of 35 mm as shown in table 2. Based on the measured data in this study (table 2), the Reynolds number Re is 1983, and the reduced frequency k is 0.75. The advance ratio, defined as $J = U_{ref}/(2\Phi fl)$, is 0.32, where Φ is the stroke amplitude of the forewing, with the value about $120 \pm 2^\circ$ as measured in this study.

The vortex structure in this study is identified by the Q -criterion [36], which has the following form for incompressible flow:

$$Q = \frac{1}{2} (\|\boldsymbol{\Omega}\|^2 - \|\mathbf{S}\|^2), \quad (2.2)$$

where $\boldsymbol{\Omega}$ and \mathbf{S} are respectively antisymmetric (vorticity tensor) and symmetric parts (rate-of-strain tensor) of velocity gradient $\nabla \mathbf{u}$. Then, the vortex is defined as a spatial region where the vorticity tensor dominates ($Q > 0$).

2.4. Evaluation of instantaneous power

The instantaneous power calculations on a hovering or forward-flying insects have been carried out based on experimental measurements [37,38] or numerical studies [35,39]. In our study, the power is estimated in the same way as that used for fruit flies [37] and for hawkmoths [40]. The instantaneous aerodynamic power is the power needed to overcome air resistance, and is defined as the surface integration of the inner product between the pressure and the velocity in each discretized element

$$p_{Aero} = - \iint p \mathbf{n} \cdot \mathbf{u}_c ds, \quad (2.3)$$

where \mathbf{n} and ds are the unit normal direction and the area of each surface element, respectively. Recalling that the Reynolds number here is far greater than 1, the power contribution from shear stress is negligible compared with that from normal pressure.

The inertial power, representing the power used to accelerate the wing, is given by

$$p_{\text{Iner}} = \iint \bar{\rho}_w \bar{h} \frac{d\mathbf{u}_c}{dt} \cdot \mathbf{u}_c ds, \quad (2.4)$$

where $\bar{\rho}_w$ and \bar{h} are the averaged density and thickness of cicada wings. Here, $\bar{\rho}_w = 2.3 \text{ g cm}^{-3}$ is used [41]. The thickness \bar{h} was then calculated to be $11.4 \text{ }\mu\text{m}$, which is in the same order of magnitude as the measurement [41]. In equations (2.3) and (2.4), \mathbf{u}_c is the velocity at the pressure centre or at the mass centre of each discretized wing element. Because over 1000 triangular elements were used to discretize the wing surface, it is reasonable to assume that the pressure centre and the mass centre of the element coincide to simplify the calculation. The total mechanical power used to move the wing is then the sum of the aerodynamic power and the inertial power, i.e.

$$p_{\text{total}} = p_{\text{Aero}} + p_{\text{Iner}}. \quad (2.5)$$

The mechanical power can be further normalized by flight muscle mass [35,37,39], which gives

$$p^* = \frac{p_{\text{total}}}{M_m}, \quad (2.6)$$

where M_m is the mass of flight muscle. The flight muscle mass of fruit fly (*Drosophila melanogaster*) is assumed to be 30% of the body mass [38]. Literature about the flight muscle mass of Cicadidae is relatively limited. In a study of the flight musculature of *Fidicina mannifera*, a cicada species in South America, the flight muscle is assumed to be 35% of the total body mass M [42]. This value was later confirmed and used for other cicada species, such as *Dorisiana bonaerensis* and *Quesada gigas* [43]. Owing to the lack of solid data on flight muscle mass of *Tibicen linnei*, we used 35% as the ratio of the flight muscle mass to the body mass.

3. Results

3.1. Flight trajectory

Over 80 cicada videos have been taken, from which the one closest to the forward flight is selected for this study. The body displacement is shown in figure 3, in which the Y-axis is the vertical direction pointing upwards, and the positive X-axis is aligned with the flight direction. The vertical displacement in the shaded region in figure 3 is around 1–2 mm, which is within the order of 1/15th of the body length. The horizontal displacement of the flight in the shaded region is, however, in the order of 5/3rd of body length. Hence, it is reasonable to ignore the climbing, and to assume that the cicada was flying forward. The body pitching angle χ is defined as the inclination angle between the horizontal and mid-frontal plane of the cicada body [29]. For the cicada studied in this paper, the body pitch angle χ is measured as $49 \pm 2^\circ$.

3.2. Wing kinematics

The wing kinematics was obtained from the phase average of the three-dimensional reconstruction of the three stroke cycles in figure 3. Using the right wings as an example, the wing kinematics in terms of three Euler angles is shown in figure 4. At the beginning of the downstroke, the forewing stroke angle is $-80 \pm 2^\circ$, indicating that the forewing was almost longitudinally aligned with the body. The hindwing

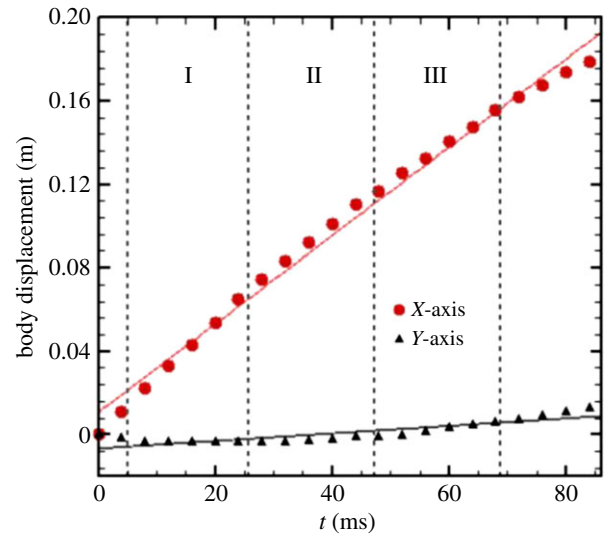


Figure 3. Body displacement of the cicada during forward flight, surface reconstructions were done for three strokes. (Online version in colour.)

lags behind the forewings by an approximately 15° stroke angle. The forewing stroke angle approaches to $45 \pm 1.5^\circ$ at the end of the downstroke. The hindwing stroke angle varies in a range from $-80 \pm 3^\circ$ at the beginning of the downstroke to $42 \pm 2^\circ$ at the end of the downstroke. The forewing deviation angle varies around zero with an amplitude of $10 \pm 0.5^\circ$, whereas the hindwing deviation angle varies between $-14 \pm 0.4^\circ$ to $-22 \pm 0.4^\circ$. The pitch angles measured at each mid-wing are shown in figure 4. The pitch angle of the forewing varies more dramatically than that of the hindwing during the whole stroke period. The former varies from $44 \pm 2^\circ$ to $133 \pm 2^\circ$, whereas the latter changes from $76 \pm 1^\circ$ to $112 \pm 2^\circ$. The stroke of the forewing (represented by the mid-wing section) over a full cycle viewed in the wing–root coordinate system is presented in figure 5a, in which the dotted line indicates the direction of the mean stroke plane, $13 \pm 0.5^\circ$ with respect to the horizontal plane. The effective angle of attack α_{eff} is the angle between the chord and resultant velocity composed of the mid-wing flapping velocity U_{flap} and the free stream velocity $U_\infty (= -U_{\text{ref}})$. The variation of α_{eff} over a stroke cycle is presented in figure 5b. Figure 6 shows the side view of reconstructed wing motion at some time instants. Dramatic wing deformation can be seen over a cycle.

3.3. Vortex development

CFD simulation was conducted using the kinematics of the wings and the body from the three-dimensional surface reconstruction. The vortex formation over a stroke cycle is shown in figure 7, in which the vortex structures are identified by the iso-surface of Q -criterion ($Q = 10$). The left and middle columns present the back view and top view vortex structures, respectively, coloured by the spanwise (transverse) vorticity. The right column is the projection view, coloured with the stream-wise vorticity. The stroke cycle starts from the downstroke of forewings, which are instantaneously aligned almost longitudinally with the cicada body (stroke angle is around -80°). The hindwings lag behind the forewings by an approximately 15° stroke angle, and are therefore in their pronation. At the onset of the downstroke (figure 7a), an LEV is uniformly distributed along each leading edge. A forewing starting vortex

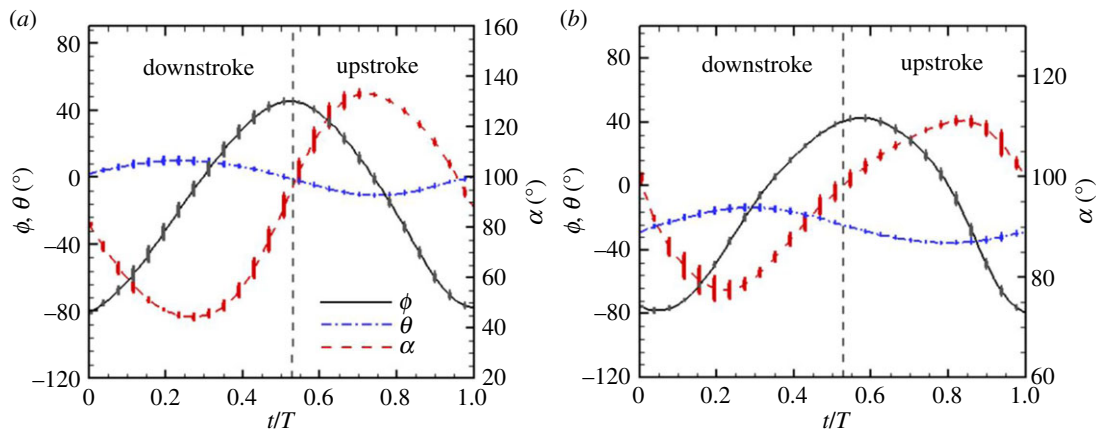


Figure 4. Stoke angle (0° lateral, downstroke positive), deviation angle (upward positive) and pitch angle (rotation around wing span, smaller than 90° when leading edge is forward) for the forewing (a) and the hindwing (b). (Online version in colour.)

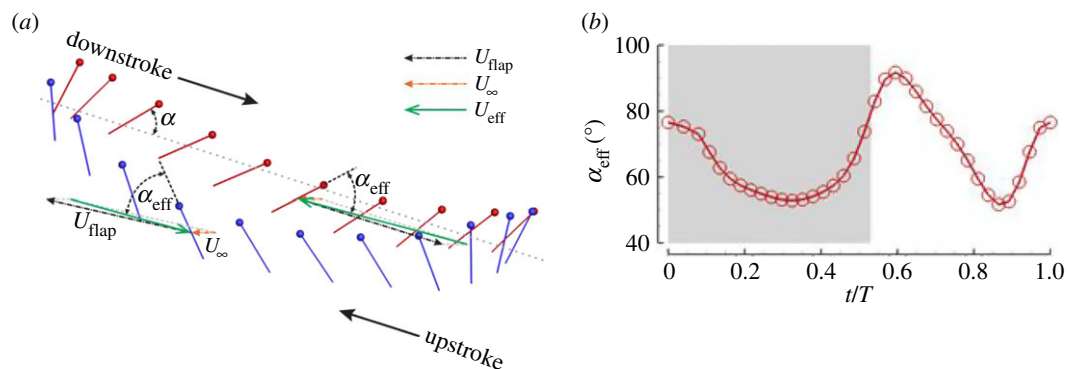


Figure 5. Pitch angle (α) and effective angle of attack (α_{eff}) of the forewing during downstroke and upstroke (a); α_{eff} of the forewing over a full stroke cycle. The leading edge is denoted by a dot. The dotted line indicates the direction of the mean stroke plane (b). The downstroke is shaded. (Online version in colour.)

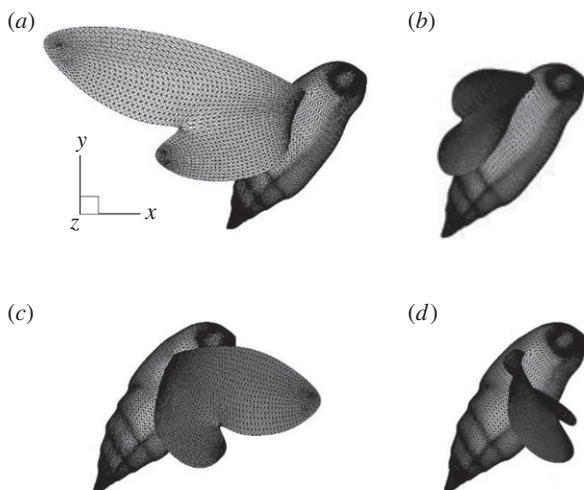


Figure 6. Wing motion during a stroke. (a) Start of downstroke; (b) mid-downstroke; (c) start of upstroke; and (d) mid-upstroke.

(FSV) is formed along the extruded forewing trailing edge (part of which is hooked with the leading edge of the hindwing). The LEV connects to the FSV through the forewing tip vortex (FTV). On each hindwing, a trailing edge stopping vortex (TSV) is created and is about to be shed during the pronation.

As the wings further stroke down (figure 7b), a three-dimensional LEV develops owing to the onset of wingtip vortices [35]. A hindwing starting vortex (HSV) forms at the

hindwing trailing edge. The two trailing edge stopping vortices (zoomed-in view in the electronic supplementary material, figure S2) are detached and approach to the cicada centre plane, instead of moving downstream. Surrounding the cicada wing, the LEV, FTV and trailing edge vortices (FSV and HSV) all together form a horseshoe-like vortex structure. However, it is unstable and may deform and break down owing to the wing shape and complex wing kinematics.

At the mid-downstroke (figure 7c), the LEV is fully developed and lift reaches the maximum. A cone-shaped FTV is formed on the dorsal surface of the wing, on which a low-pressure region is created and enhances the lift generation. The starting vortices (FSV and HSV) from the forewing and the hindwing are merged. Near the root of the hindwing, a wing root vortex (WRV) is generated on each side of the cicada. A closed vortex ring, composed by the FTV, trailing edge vortex and the WRV, is formed on each side of the body. The vortex ring has a small inclination angle with respect to the flight direction, and thus induces downwash flow. Another distinctive feature is that a vortex structure is developed from the cicada thorax (named as thorax vortex and denoted as TXV), and is shed onto the wings at the mid-downstroke. This may provide another mechanism to enhance the lift generation.

At the end of the downstroke (figure 7d), the vortex rings are elongated. A strong tip vortex is developed from the hindwing (HTV), entangling with forewing tip vortices (FTV); a zoomed-in view can be seen in the electronic supplementary material, figure S3. One distinctive feature is the

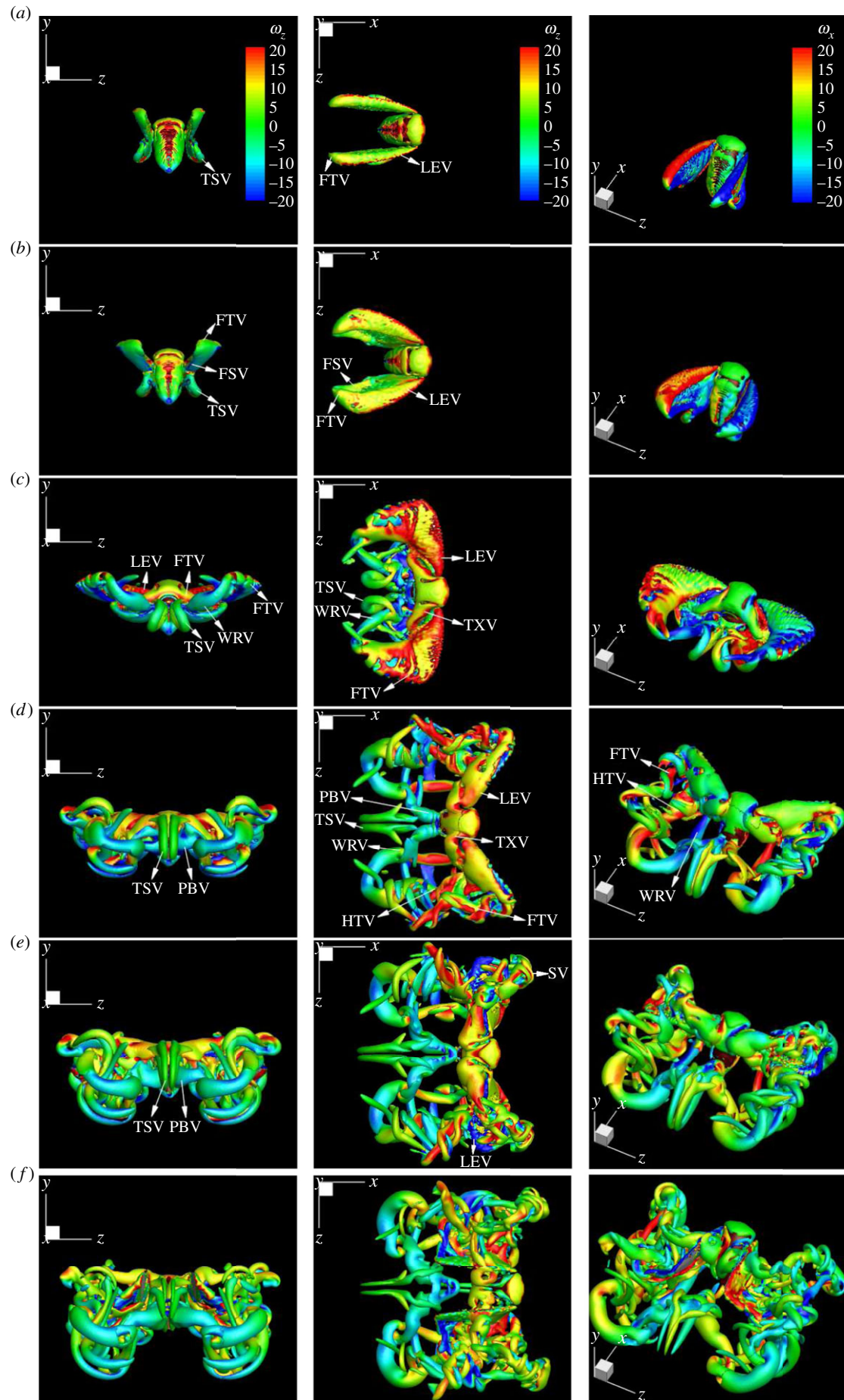


Figure 7. (a–f) Time course of vortex development, visualized by the Q -criterion. The left and middle columns are back view and top view, respectively, and the vortex structures are coloured by spanwise vorticity. The right column shows the structures in projection view, coloured by streamwise vorticity. Colour bars in the first row apply to figures in the same column.

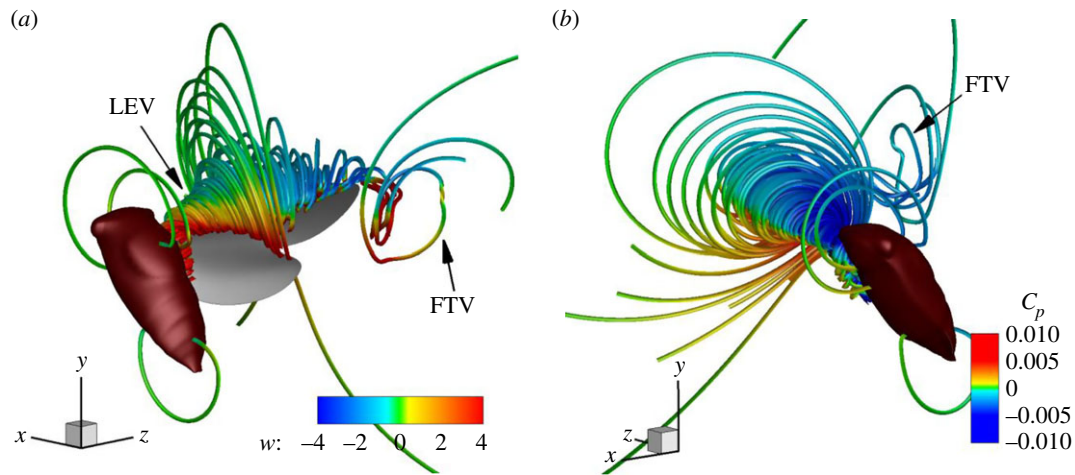


Figure 8. Streamline around the leading edge at mid-downstroke. Only the right wing is presented for a clearer view.

clamper type of vortex tubes that emanate from the posterior region of the body (PBV) on the one end, and clasp the WRV on the other end. From the top view, we can see that the tip vortex and the WRV are aligned in the direction of forward flight, in contrast to the circular vortex ring of hovering insects [35].

At the mid-upstroke (figure 7e), the vortices emanating from the posterior cicada body are elongated and intertwined with the wing root vortices. A starting vortex (SV) shed forwardly during supination can also be seen. Although the wings could potentially extract energy from the SV if correctly orientated [16], no interaction between the SV and the wings was found in this study on cicada forward flight. However, we can see the forewing cutting through the downstroke-generated LEV during the upstroke. The downstroke-generated LEV is stable and most of it attaches to the wing until the mid-upstroke. This result is also consistent with the observation of bumblebees [21]. In the upstroke, new LEV and vortex rings can still be found at the ventral side of the wing, but their strengths are much smaller than those generated in the downstroke.

At the end of upstroke (figure 7f), the vortex tube previously formed in the downstroke from the posterior cicada body has been detached, with each arm hooked to the vortex ring generated in the downstroke. Eventually, the vortex ring in each side of the body will merge with the PBV, and potentially form one big vortex ring after several stroke cycles.

Streamlines near the leading edge and the wingtip at the mid-downstroke are shown in figure 8. The streamlines in the left and right columns are, respectively, coloured by the spanwise velocity and the non-dimensional pressure coefficient. The spiral streamlines grow in the spanwise direction from the wing root to the mid-wing. The spiral size decreases from the mid-wing to the wingtip. The streamline near the wingtip bends and joins the wingtip vortex (FTV). Low pressure on the dorsal wing surface can be clearly seen in figure 8b.

Figure 9 shows the LEV structure at the mid-downstroke at four slices, respectively, cut at 15%, 40%, 65% and 90%, along the spanwise direction from the wing root to the wing tip. The double LEV structure was observed on the 40% and 65% spanwise locations, and a single vortex was found near the wing tip (90%). The second vortex on the slice at the 15% spanwise location was the thorax-generated vortex (TXV). In other words, a single LEV was found near the wing root region (15%).

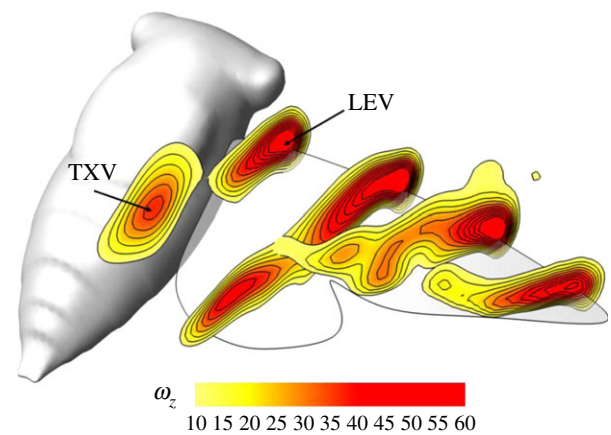


Figure 9. Leading edge vortex at the mid-downstroke, coloured by the spanwise vorticity. (Online version in colour.)

3.4. Surface pressure distribution

The aerodynamic pressure, which is perpendicular to the local wing elements, is projected in horizontal and vertical directions to indicate the horizontal and vertical force distributions over the wing surface (figure 10). The aerodynamic pressure is non-dimensionalized by the wing load (the ratio of the cicada weight to the total wing surface area). Figure 10a(i) shows the back view (the cicada flies into the paper) of projected pressure distribution at the mid-downstroke, at which the whole wing experiences drag. It is interesting to note that the minimum drag is near the forewing leading edge and the wingtip, recalling that the speed at the wingtip is highest and the pressure should be high at first thought. This can be explained by considering the small pitch angle near the wingtip region and therefore the small projection area in the flight direction. From figure 10a(ii), it can be seen that most of the lift is generated by the forewing, especially in the region between 20% and 90% from the wing root to the wingtip. Figure 10b shows the back view pressure distribution at the mid-upstroke, at which thrust is generated by the whole forewing and front half of the hindwing. Drag is distributed in the second half of the hindwing. In figure 10b(ii), the maximum lift is generated at the tip of the forewing. Although the pressure projected in the vertical direction is positive in most areas of the wing surface, the resultant lift is apparently smaller than that at mid-downstroke (compared with figure 10a(ii)). Figure 10c displays

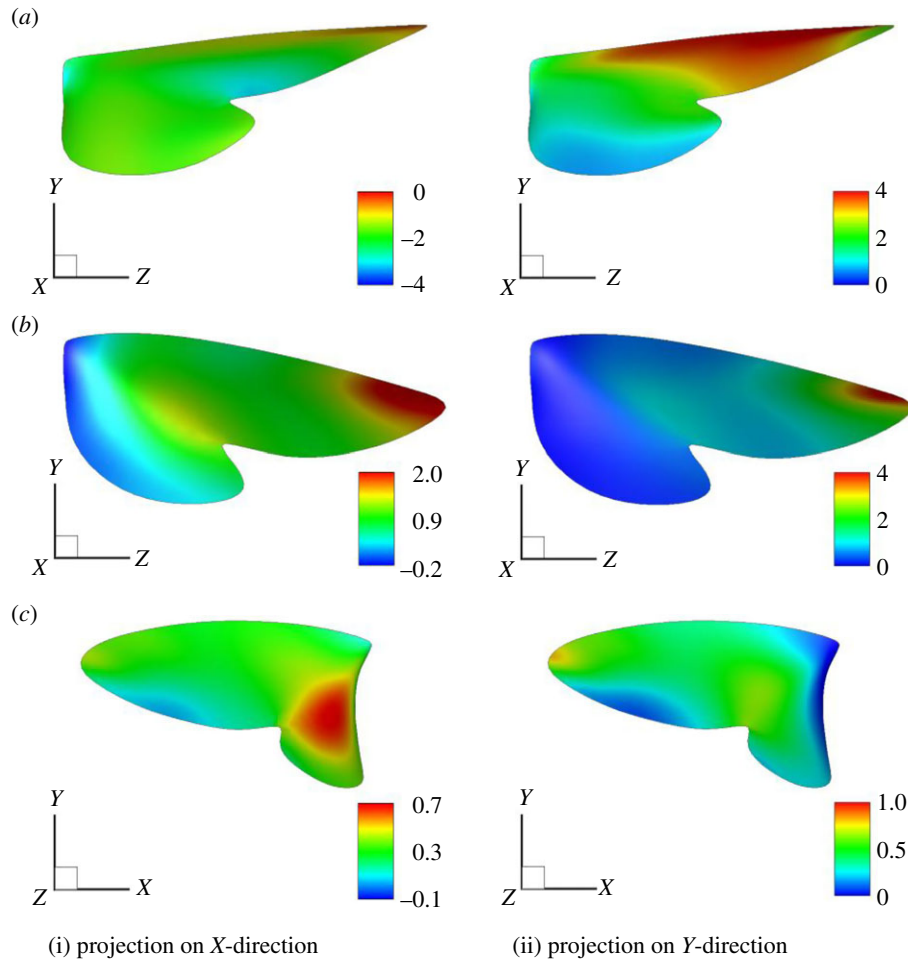


Figure 10. Surface pressure distribution projected on the X -direction (left column) and the Y -direction (right column). (a) Mid-downstroke (Y - Z plane); (b) mid-upstroke (Y - Z plane); and (c) before the end of the upstroke (X - Y plane).

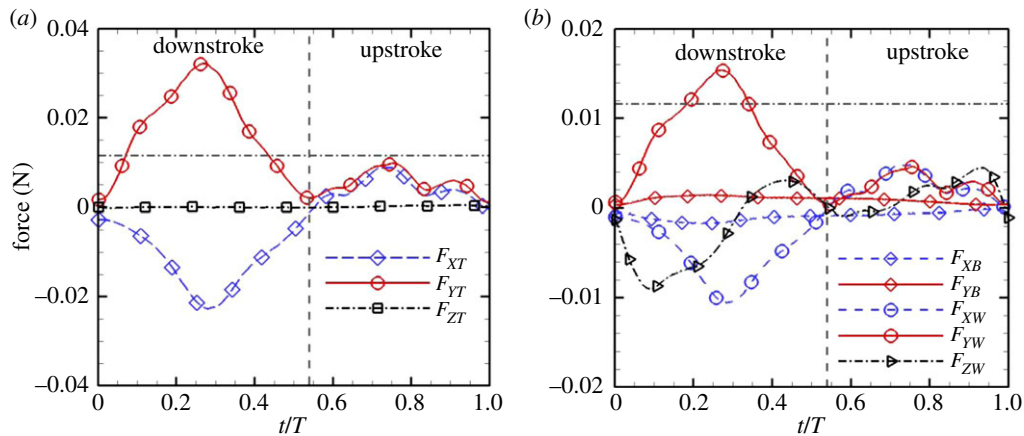


Figure 11. Force generation in one stroke. (a) Total force (F_{XT} , F_{YT} , F_{ZT}) is composed of forces from wings in both sides and the cicada body. (b) Force generated by the right wings and the body. (Online version in colour.)

the side view (the cicada flies from the left to the right) thrust and lift distribution around the end of the upstroke. It can be seen (figure 10c(i)) that thrust is mainly produced by the hindwing, especially near and below the coupling region between the forewing and the hindwing, even though the magnitude of the thrust is small compared with that in mid-upstroke.

3.5. Aerodynamic force

The instantaneous aerodynamic force is obtained through the surface integration of the pressure and shear stress over

the wing and the body. The lift, thrust and side force are then calculated by projecting the integrated force on the vertical (Y), horizontal (X) and spanwise (Z) directions. The total instantaneous vertical force (F_{YT}), horizontal force (F_{XT}) and side force (F_{ZT}), as shown in figure 11, are the sum of forces from all the wings and the body. The vertical dashed line separates the flapping cycle into the downstroke and upstroke, which are asymmetric in terms of stroke cycle. The downstroke took about 53% of the stroke cycle, whereas the upstroke accounted for 47%. The time ratio between downstroke and upstroke was about 1.33. The weight of the cicada is indicated by the

horizontal dash-dotted line. The integration of the total instantaneous vertical force in figure 11a showed that 79% of total lift was generated in the downstroke, whereas the remaining 21% was generated in the upstroke. The averaged vertical force \bar{F}_{YT} during one stroke cycle was 11.96×10^{-3} N. Considering that the weight of the cicada was 11.57×10^{-3} N, the calculated vertical force from our simulation gives 96.7% accuracy. The blue curve F_{XT} in figure 11a is the force experienced by the cicada in the flight direction, with negative and positive values indicating drag and thrust, respectively. It showed that the cicada experienced drag in the downstroke, and produced thrust in the upstroke. The time-averaged force \bar{F}_{XT} during the whole stroke cycle was -4.282×10^{-3} N. Thus, the cicada was decelerating, which is consistent with the video record of body displacement and kinematics. Except for the short instants around pronation, the total side force F_{ZT} was almost zero during the stroke, which proved that the cicada was in forward flight.

The forces on the cicada body and right wings (denoted by subscripts B and W, respectively) are shown in figure 11b. The vertical force on the body F_{YB} is positive throughout the wing stroke (recalling that the body angle is $49 \pm 2^\circ$ in this study). The vertical force F_{YW} (the sum of forces on the forewing and hindwing) reaches its maximum near the mid-downstroke, at which F_{YB} is about one order of magnitude smaller than F_{YW} (9.2%). At the mid-upstroke, F_{YB} is about 17.7% of F_{YW} . The lift generated by the body is comparable in magnitude to the lift from the wings only near the stroke reversal, at which the wing pitch angle is momentarily high. Generally, F_{YB} plays a negligible role in lift generation when both wings are considered. However, because F_{YB} is positive throughout the wing stroke, its accumulation always contributes to the lift generation. Over the complete stroke cycle, the lift production from the body takes 7.45% of the total lift generation. The cicada body experiences negative horizontal force F_{XB} during the whole stroke. The averaged force \bar{F}_{XB} accounts for 20.8% of the total drag experienced by the cicada. The side force on right wings F_{ZW} is also presented in figure 11b. During the downstroke, F_{ZW} switches sign when the wings pass over the Y' -axis in figure 2. F_{ZW} in the upstroke shows a similar trend, but with a smaller magnitude than that in the downstroke.

3.6. Power estimation

The aerodynamic power and inertial power over the course of a stroke cycle are estimated using equations (2.3) and (2.4), respectively. The total specific mechanical power, which is the power normalized by the flight muscle mass, is shown in figure 12. The instantaneous aerodynamic power is always positive over the stroke cycle, although its value is quite small near stroke reversal. The shape of instantaneous aerodynamic power resembles the shape of aerodynamic forces. In the downstroke, the aerodynamic power plays a dominant role, and obtains the maximum near the mid-downstroke. In the upstroke, the aerodynamic power is much smaller than that in the downstroke, and its highest value occurs around the mid-upstroke. The averaged aerodynamic power in the full stroke cycle is 48.5 W kg^{-1} , composed by 42.7 and 5.8 W kg^{-1} during the downstroke and the upstroke, respectively.

The inertial power can be both positive and negative in the stroke cycle. At the beginning of the downstroke, the inertial power increases sharply owing to the wing

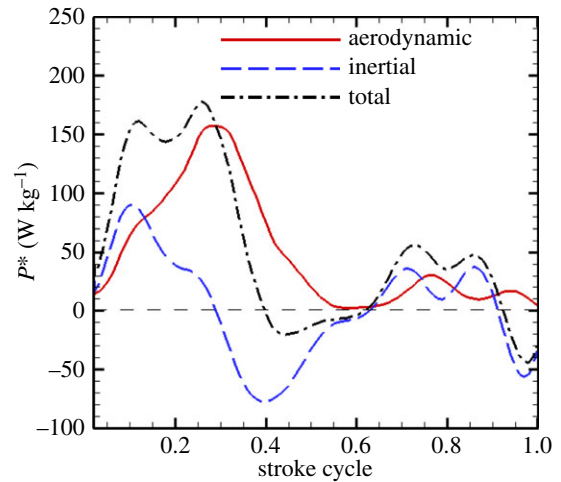


Figure 12. Instantaneous specific power in a stroke cycle of cicada flight. (Online version in colour.)

acceleration. It then decreases until the mid-downstroke, after which it reverses the sign. During the ventral reversal (with a value of 0.55–0.6 in the stroke cycle), the inertial power is slightly negative. In the upstroke, the inertial power is positive over 75% of the duration of the upstroke; it then reverses sign when the wing decelerates near the end of upstroke. Assuming there is no energy cost when the wing decelerates, the averaged inertial power over the full stroke cycle is 23.2 W kg^{-1} , with 16.8 and 6.4 W kg^{-1} for the downstroke and upstroke, respectively.

The total mechanical power rises sharply when both the aerodynamic power and inertial power are positive in the first half of the downstroke. As the aerodynamic power decreases and the inertial power reverses sign in the second half of the downstroke, the total mechanical power decreases. It becomes negative during the end of the downstroke. In the upstroke, the total mechanical power presents the same trend in sign switching as in the downstroke. As suggested by Dickinson & Lighton [44], insects can actually supply less power than the total mechanical power to maintain flight, because the negative mechanical power can be stored by insects and recovered at the start of the next stroke. The cicada in this study seems to be taking advantage of the negative mechanical power near each stroke reversal.

4. Discussion

4.1. Force generation

Using a model wing of fruit fly, Sun & Wu [39] numerically studied aerodynamic force generation of a fruit fly in forward flight. They found that 75–80% of lift was generated in the downstroke at low speed (advance ratio $J=0.13$). As J increased to 0.27, an even greater percentage of lift was contributed by the downstroke. In our study of cicada flight with an advance ratio of 0.32, 79% of lift was generated in the downstroke. The results of the fruit fly model wing are qualitatively consistent with our study on real cicada flight.

For the thrust generation, two mechanisms were proposed [45]. One was the lift-based mechanism, in which thrust is generated by the redirection of lift through forward tilting of the wing stroke plane [46]. The second was the drag-based thrust generation, the wing paddling as discussed in the flight of fruit flies [20]. In the flight of cicadas, we also

Table 3. Power comparison on several insects. The unit of mass-specific power is W kg^{-1} . 'fwd' means forward flight. p^* and p_{Aero}^* stand for the muscle-mass-specific mechanical and aerodynamic power, respectively. p_{BM}^* and $p_{\text{Aero,BM}}^*$ are the body-mass-specific mechanical and aerodynamic power, respectively. The range of specific mechanical power is calculated from the two extremes of full or zero elastic energy storage. In [40], mass of flight muscle is assumed to contribute 23% of the total body mass.

insects	flight	f (Hz)	l (mm)	J	p_{Aero}^*	p^*	$p_{\text{Aero,BM}}^*$	p_{BM}^*
fruit fly [37]	hover	210–227	2.3–2.48	0	97	97–115	29.1	29.1–34.5
fruit fly [35]	hover	218	2.39	0	89.3	89.3–146.2	29.8	29.8–48.7
hawkmoth [40]	hover	26.1	47.6	0	90	155	20.7	35.7
fruit fly [39]	fwd	240	3.0	0.32	—	93.7	—	28.1
bumblebee [17]	fwd	132	13.7	0.34	50/83	50/80–127/150	15/25	15/25–38/45
cicada (this study)	fwd	47.6	35.1	0.32	48.5	48.5–71.7	16.9	16.9–25.1

found that cicada wings experience drag during downstroke, and generate thrust in the upstroke by pushing back the wings. As shown in figure 5*b*, the effective angle of attack α_{eff} was high in the time range of $t/T = 0.6$ – 0.85 , indicating the generation of thrust after wing supination and during most of the upstroke. Wing paddling hence may be taken by both small and big insects to propel them forward. It is also interesting to note that thrust generation during the upstroke is fulfilled by a combination of the forewing and the hindwing in a temporal manner. During most of the stage in the upstroke, thrust is mainly generated by the forewing (e.g. figure 10*b*(i)). Near the end of the upstroke, as the forewing pronates for the next stroke cycle, the hindwing takes over and contributes the thrust generation (figure 10*c*(i)).

Willmott & Ellington [19] suggested that *M. sexta* uses various wing areas for different aerodynamic roles. In the cicada flight, we noted that even the same wing portion may perform differently in aerodynamics depending on the stage of the wing stroke. For example, the forewing distal region produces high lift at the mid-downstroke (figure 10*a*(ii)), whereas it becomes a principal region of thrust generation near the mid-upstroke (figure 10*b*(i)).

4.2. Power expenditure

The power consumption during hovering or forward flight was previously investigated using experimental or computational techniques for various insects [17,35,37,39,47,48]. In the cicada's free flight, the inertial power increases faster than the aerodynamic power at the beginning of both downstroke and upstroke. This result is qualitatively consistent with that from studies on fruit flies [35,37]. The sharp increase of inertial power at the beginning of each half-stroke may be ascribed to the pronation or the supination during wing stroke reversals.

We note that both the aerodynamic power and the total mechanical power in the downstroke are significantly higher than those in the upstroke. It is suggested that the cicada in free forward flight ($J = 0.32$) consumes much more power in the downstroke than in the upstroke to provide enough lift supporting the weight, and to overcome drag to move forward. In studies of fruit fly forward flight, the same phenomenon of higher power expenditure during downstroke was observed [39]. Both results indicate that insects do much more work in the downstroke than in the upstroke during forward flight.

Table 3 presents some data of power requirement for several insects. The range of mechanical power is estimated based on two extreme cases, i.e. full and zero elastic energy

storage. For example, in the study of Fry *et al.* [37], the minimum and maximum muscle-mass-specific mechanical power p^* are 97 and 115 W kg^{-1} , respectively, by considering full and zero elastic energy storage. The mechanical power for the fruit fly at $J = 0.32$ in table 3 is deduced from Sun & Wu [39], in which they also found that the power requirement for flight at slow and medium speed is just a little smaller than that needed for hovering. However, the power requirement increases rapidly at higher speed. Data regarding bumblebees are adapted from Dudley ([17], indices BB01 and BB02), by assuming that the aerodynamic power required by BB01 and BB02 are identical since the mass and wing size of the two bumblebees are very close. The two values separated by a forward slash (e.g. 50/83 in p_{Aero}^*) were calculated from two mean profile drag coefficients of 0.1 and 0.3, respectively. Dudley [17] suggested that mechanical power is independent of flight speed from hovering to advance ratio around 0.6. More accurately speaking, the power curves show very shallow minima at medium flight speed. In our study of cicada, we have only one flight speed corresponding to $J = 0.32$. Given the fact that the mechanical power is weakly dependent on the flight speed of fruit flies and bumblebees, we speculate that the mechanical power consumption for cicada flight is also insensitive to the flight speed in the range from hovering to medium speed, although the former may need a little higher power than the latter.

We note in table 3 that, as the size and weight of insects increase, both the aerodynamic and mechanical power per unit mass decrease. It has been suggested [27] that the mass is proportional to l^3 , and that the aerodynamic power per unit mass is proportional to fl . Although the data in table 3 do not exactly fit the two formulae aforementioned, general comments made by Ellington [27] about the variation of wing length and flapping frequency with weight maintenance at a certain power are still valid. As a result [27], the combination of longer wing and lower flapping frequency may be the feasible strategy taken by heavy insects (e.g. cicadas) to support their weight. This combination also gives the reason for the smaller body-mass-specific mechanical power (p_{BM}^*) of heavier insects. The flight speed, which is proportional to the flapping velocity ($\sim fl$) [27], hence is sacrificed. This explains why fruit flies live a more vigorous life than cicadas.

4.3. Leading edge vortices

The flow topology over an insect's wings and its thorax was categorized in previous studies [6,49]. For insects with slender

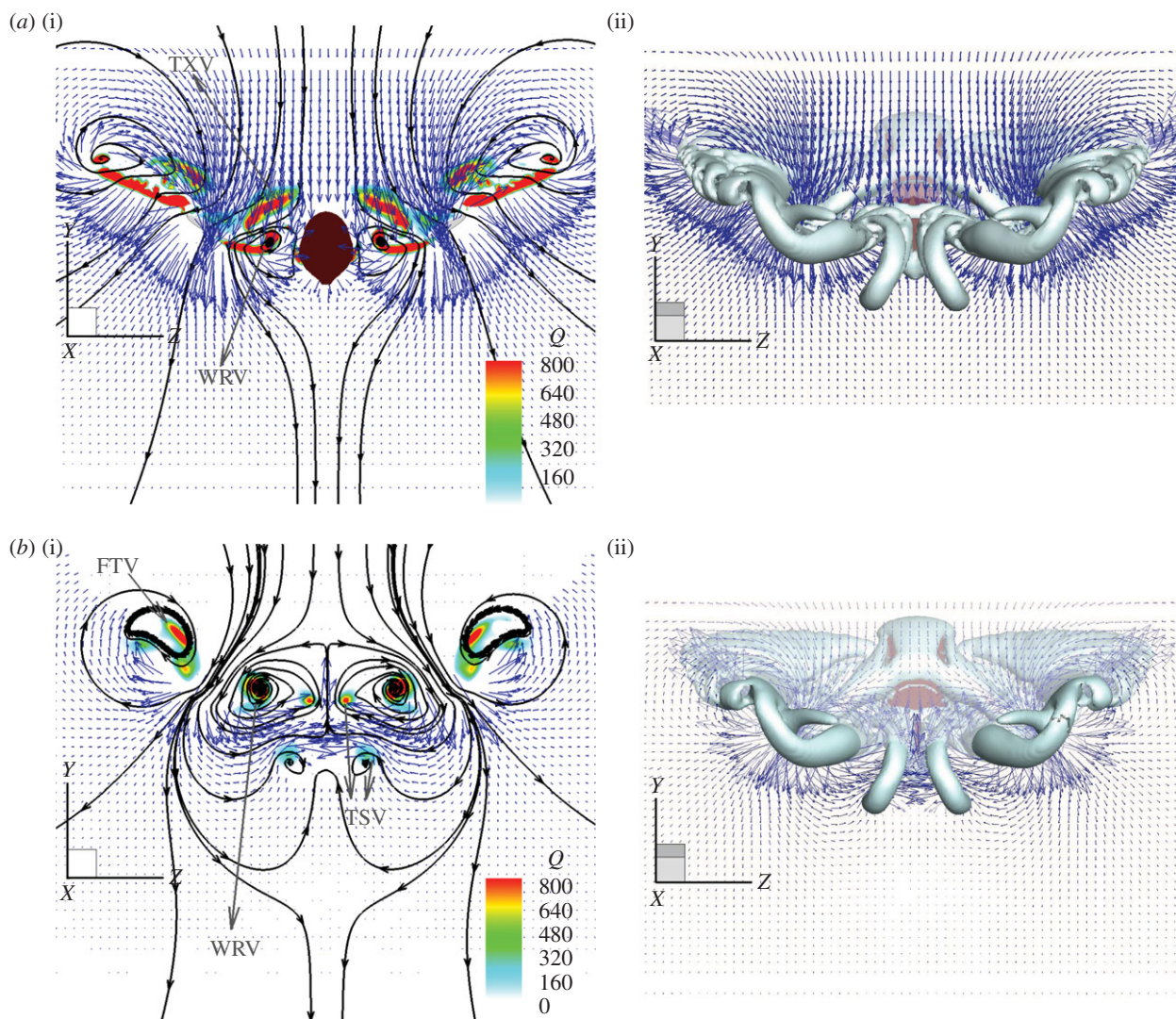


Figure 13. Transverse plane cut at mid-downstroke. (a) Cut through wing and body and (b) cut through the near wake (no wings or body being cut). (i) Contour of the Q -criterion, velocity vector and two-dimensional streamline seen from the back view. (ii) Vortex structure ($Q = 20$), and the velocity vector. The view angle is different from that in column (i), and is adjusted to give a better view of the vortex structure. The velocity vectors are three dimensional, and are drawn at every three grid points only. (Online version in colour.)

and intermediate body widths, the LEV was found to continuously cross the thorax and runs along each wing to the wingtip in tethered hawkmoths [6], free-flying dragonflies [12] and free-flying butterflies [16]. On the other hand, in forward flight of insects with wide bodies such as cicadas, the vortex structures at the leading edge and the centreline of the body are distinct from previous discussions. The three-dimensional vortex structure during the downstroke (figure 7*b–d*) clearly shows that the LEVs on the right and left wings develop separately. At the mid-downstroke (figure 7*c*), a conical-shaped LEV is formed starting from each wing base, where a surface-bound focus exists. The absence of linkage between the LEVs in a hawkmoth was considered as a transient state, and LEVs could be connected once flow over the thorax had separated [6]. This conjecture can be possible for insects with slender and intermediate body width. In the flight of a cicada, whose body is much wider than that of a hawkmoth [6], the LEVs remain unconnected throughout the course of the downstroke (figure 7*d*).

In some more recent studies, it was found that multiple LEVs were generated on the wings of real hawkmoths [24], and in a wing model of fruit fly [32]. In both studies, a single LEV occurs at the inner wing and multiple LEVs were observed

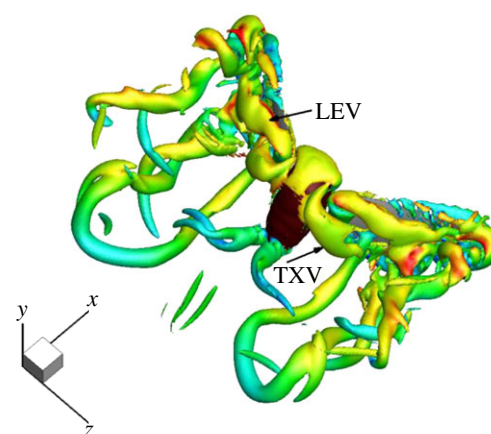


Figure 14. Vortex structure at the end of downstroke (coloured by unified spanwise vorticity, colour max/min = ± 4). (Online version in colour.)

in the mid-wing region. Our results of LEV structure along the cicada wingspan are qualitatively consistent with these studies [24,32]. The cicada thorax-generated vortex was also found on the slice cut at the 15% spanwise location, indicating the importance of wing–body interactions in insects with a wide body.

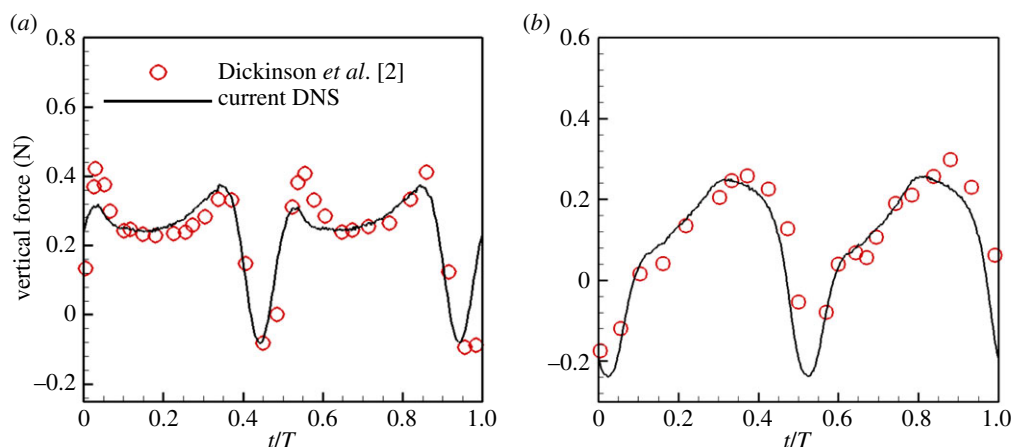


Figure 15. Lift production from this study and previous works on a robotic fruit fly wing. (a) Advanced rotation. (b) Delayed rotation. (Online version in colour.)

It is also noted that the strength of the front LEV is weaker than that of the second LEV in hawkmoth flight [24]. In cicada flight, the front LEV is stronger than the second LEV at both the 40% and 65% spanwise locations. This distinction may be ascribed to differences in wing kinematics and wing shape between hawkmoths and cicadas.

4.4. Wing root vortex and two-vortex-ring structure

In free flight of bumblebees, it was observed that wing root vortices were formed by the inflection of the LEV [21]. In the flight of a cicada, whose body width is wider than that of bumblebee workers (table 1), the WRV is also found. However, it is generated directly from the wing root (figure 13), in contrast to its formation from the inflection of LEV in bumblebees. Figure 13a(i) shows the velocity vector and two-dimensional streamlines in a transverse plane cutting through the wing and part of the body. The LEV, TXV and WRV actually form a jet through which strong downwash flow is induced near the mid-wing region (figure 13a(ii)). Figure 13b(i) is the velocity vector in a transverse plane half a body length behind the cicada, at which the trailing edge stopping vortices (TSVs) are cut. The pair of TSVs approaches to the centre plane owing to self-induction (figure 13b(ii)). The induced flow by TSVs can potentially enhance the formation and development of the WRV, and therefore indirectly help the downwash. The WRV induces upwash flow proximal to the hindwing and the body, but the affected region is far smaller than the estimated upwash region generated by bumblebees [21].

It is interesting to note that the vortex structure shown in figure 13b(i) is similar to the experimental results of free-flying beetles [23] (figure 1 therein), in which the wing tip vortex and near-body vortex were called as 'Wt' and 'Bv', respectively. Their counterparts in this study were denoted by 'FTV' and 'WRV', respectively. It can be seen from both studies that vortices emanating from the wing tip and wing root regions contribute to the downwash flow. In the flight of beetles, a vortex produced by the elytra helps the downwash. In the cicada flight, the downwash is enhanced by the TXV generated from the thorax.

A contralateral vortex ring is formed on each body side by the wing tip vortex, trailing edge vortex and wing root vortex. Therefore, a two-vortex-ring structure is formed in the near wake, as shown in figure 14. In addition, even at the end of the downstroke, the right- and left-side LEVs are still disconnected. The vortex shed from the cicada thorax (TXV) during upstroke is prone to combine with WRV, instead of connecting to LEVs.

Note the two-vortex rings were clamped by the posterior body vortices (PBVs), generated from the tail of the cicada.

For insects with slender bodies, only one vortex ring was found owing to the connection between LEVs on each side of the body [6,12,35]. As the body width of insects increases, for example the bumblebee, wing root vortices are formed through the inflection of LEVs [21]. In the flight of the cicada, whose body is even wider, two-vortex rings are generated, whereas the wing root vortices directly emanate from the wing bases. The two-vortex rings, entangled with the PBVs, are stable structures even at the end of a full stroke cycle (figure 7f). Eventually, the WRVs and PBVs may merge and the two-vortex rings can combine to form one bigger ring, after a few stroke cycles. The two-vortex ring structure was considered as a trade-off between control authority and aerodynamic efficiency [21]. However, the two-vortex ring may not be necessarily aerodynamically inefficient, especially for insects with wide bodies. The two-vortex-ring structure, reinforced by the vortices from the thorax, can induce strong downwash over most of the wing span area. The independent LEV, combined with the two-vortex-ring structure in the near flow field, might be a natural adaption to provide both control flexibility and aerodynamic forces for cicadas, and some other insects with wide bodies.

Acknowledgements. All the experiments and initial computational analysis for this paper were performed at the Department of Mechanical and Materials Engineering at Wright State University, Dayton, OH, USA. The authors are indebted to Dr Zongxian Liang for assistance with validations, to Dr Geng Liu for discussion on LEV and figure 9, to Yan Ren for help on figure 5 and figure 9, and to Zhe Ning, Chengyu Li and Zach Gaston for their videotaping.

Funding statement. This work was supported by National Science Foundation CBET-1313217 and AFOSR FA9550-12-1-0071.

Appendix A. Computational fluid dynamics solver validation

In order to demonstrate the validity of the CFD solver used in this paper, simulations of flow around a robotic fruit fly wing were conducted. The robotic wing replicates *Drosophila melanogaster* wings [3] with wing area 0.0167 m^2 , span 0.25 m , and average chord $\bar{c} = 8.79 \text{ cm}$. The wing in experiments [3] sweeps in the horizontal plane and rotates at the end of each stroke. The stroke amplitude is 160° , the angle of attack at mid-stroke is 40° and flapping frequency is 0.145 Hz . The wing is

either advanced rotated or delayed rotated by 8% of the stroke cycle with respect to the stroke reversal. The Reynolds number is 136, with the average translational velocity at the wing mid-chord 0.15 m s^{-1} . A non-uniform Cartesian grid of size $181 \times 241 \times 181$ is used in a computational domain of $30c \times 30c \times 30c$ to get domain independence results. The simulation is conducted for six flapping cycles. The vertical force coefficient during each stroke is virtually identical after the third cycle. Figure 15 shows the vertical force coefficient from

the fourth cycle for cases of advanced rotation and delayed rotation, together with the experimental results [3]. Two lift peaks are produced around the beginning and the end of the half-stroke for the case of advanced rotation, and there is only one lift peak near the end of the half-stroke for the delayed rotation case. As can be seen, our simulations capture the experimental results well. This proves that the current CFD solver can accurately predict the instantaneous force for flow past a three-dimensional flapping wing.

References

- Sane SP. 2003 The aerodynamics of insect flight. *J. Exp. Biol.* **206**, 4191–4208. (doi:10.1242/jeb.006663)
- Dickinson MH, Lehmann FO, Sane SP. 1999 Wing rotation and the aerodynamic basis of insect flight. *Science* **284**, 1954–1960. (doi:10.1126/science.284.5422.1954)
- Ellington CP. 1984 The aerodynamics of hovering insect flight. IV. Aerodynamic mechanisms. *Phil. Trans. R. Soc. Lond. B* **305**, 79. (doi:10.1098/rstb.1984.0052)
- Ellington CP, vandenBerg C, Willmott AP, Thomas ALR. 1996 Leading-edge vortices in insect flight. *Nature* **384**, 626–630. (doi:10.1038/384626a0)
- Lentink D, Dickinson MH. 2009 Rotational accelerations stabilize leading edge vortices on revolving fly wings. *J. Exp. Biol.* **212**, 2705–2719. (doi:10.1242/jeb.022269)
- Bomphrey RJ, Lawson NJ, Harding NJ, Taylor GK, Thomas ALR. 2005 The aerodynamics of *Manduca sexta*: digital particle image velocimetry analysis of the leading-edge vortex. *J. Exp. Biol.* **208**, 1079–1094. (doi:10.1242/jeb.01471)
- Henningson P, Bomphrey RJ. 2013 Span efficiency in hawkmoths. *J. R. Soc. Interface* **10**, 20130099. (doi:10.1098/rsif.2013.0099)
- Brodsky AK. 1991 Vortex formation in the tethered flight of the peacock butterfly *Inachis io* L. (Lepidoptera, Nymphalidae) and some aspects of insect flight evolution. *J. Exp. Biol.* **161**, 77–95.
- Grodnitsky DL, Morozov PP. 1993 Vortex formation during tethered flight of functionally and morphologically 2-winged insects, including evolutionary considerations on insect flight. *J. Exp. Biol.* **182**, 11–40.
- Bomphrey RJ, Henningson P, Michaelis D, Hollis D. 2012 Tomographic particle image velocimetry of desert locust wakes: instantaneous volumes combine to reveal hidden vortex elements and rapid wake deformation. *J. R. Soc. Interface* **9**, 3378–3386. (doi:10.1098/rsif.2012.0418)
- Willmott AP, Ellington CP, Thomas ALR. 1997 Flow visualization and unsteady aerodynamics in the flight of the hawkmoth, *Manduca sexta*. *Phil. Trans. R. Soc. Lond. B* **352**, 303–316. (doi:10.1098/rstb.1997.0022)
- Thomas ALR, Taylor GK, Srygley RB, Nudds RL, Bomphrey RJ. 2004 Dragonfly flight: free-flight and tethered flow visualizations reveal a diverse array of unsteady lift-generating mechanisms, controlled primarily via angle of attack. *J. Exp. Biol.* **207**, 4299–4323. (doi:10.1242/jeb.01262)
- Dudley R. 2002 *The biomechanics of insect flight: form, function, evolution*. Princeton, NJ: Princeton University Press.
- Betts CR. 1986 The kinematics of heteroptera in free flight. *J. Zool.* **1**, 303–315.
- Riley JR, Downham MCA, Cooter RJ. 1997 Comparison of the performance of *Cicadulina leafhoppers* on flight mills with that to be expected in free flight. *Entomol. Exp. Appl.* **83**, 317–322. (doi:10.1046/j.1570-7458.1997.00186.x)
- Srygley RB, Thomas AL. 2002 Unconventional lift-generating mechanisms in free-flying butterflies. *Nature* **420**, 660–664. (doi:10.1038/nature01223)
- Dudley R. 1991 Biomechanics of flight in neotropical butterflies: aerodynamics and mechanical power requirements. *J. Exp. Biol.* **159**, 335–357.
- Fry SN, Sayaman R, Dickinson MH. 2003 The aerodynamics of free-flight maneuvers in *Drosophila*. *Science* **300**, 495–498. (doi:10.1126/science.1081944)
- Willmott AP, Ellington CP. 1997 The mechanics of flight in the hawkmoth *Manduca sexta*. II. Aerodynamic consequences of kinematic and morphological variation. *J. Exp. Biol.* **200**, 2723–2745.
- Ristroph L, Bergou AJ, Guckenheimer J, Wang ZJ, Cohen I. 2011 Paddling mode of forward flight in insects. *Phys. Rev. Lett.* **106**, 178103. (doi:10.1103/PhysRevLett.106.178103)
- Bomphrey RJ, Taylor GK, Thomas ALR. 2009 Smoke visualization of free-flying bumblebees indicates independent leading-edge vortices on each wing pair. *Exp. Fluids* **46**, 811–821. (doi:10.1007/s00348-009-0631-8)
- Le TQ, Truong TV, Park SH, Quang Truong T, Ko JH, Park HC, Byun D. 2013 Improvement of the aerodynamic performance by wing flexibility and elytra: hind wing interaction of a beetle during forward flight. *J. R. Soc. Interface* **10**, 20130312. (doi:10.1098/rsif.2013.0312)
- Johansson LC, Engel S, Baird E, Dacke M, Muijres FT, Hedenstrom A. 2012 Elytra boost lift, but reduce aerodynamic efficiency in flying beetles. *J. R. Soc. Interface* **9**, 2745–2748. (doi:10.1098/rsif.2012.0053)
- Johansson LC, Engel S, Kelber A, Heerenbrink MK, Hedenstrom A. 2013 Multiple leading edge vortices of unexpected strength in freely flying hawkmoth. *Sci. Rep.* **3**, 3264. (doi:10.1038/srep03264)
- Dudley R, Ellington CP. 1990 Mechanics of forward flight in bumblebees 0.1. Kinematics and morphology. *J. Exp. Biol.* **148**, 19–52.
- Okamoto M, Yasuda K, Azuma A. 1996 Aerodynamic characteristics of the wings and body of a dragonfly. *J. Exp. Biol.* **199**, 281–294.
- Ellington CP. 1999 The novel aerodynamics of insect flight: applications to micro-air vehicles. *J. Exp. Biol.* **202**, 3439–3448.
- Grodnitsky DL. 1995 Evolution and classification of insect flight kinematics. *Evolution* **49**, 1158–1162. (doi:10.2307/2410440)
- Tobalske BW, Warrick DR, Clark CJ, Powers DR, Hedrick TL, Hyder GA, Biewener AA. 2007 Three-dimensional kinematics of hummingbird flight. *J. Exp. Biol.* **210**, 2368–2382. (doi:10.1242/jeb.005686)
- Koehler C, Liang Z, Gaston Z, Wan H, Dong H. 2012 3D reconstruction and analysis of wing deformation in free-flying dragonflies. *J. Exp. Biol.* **215**, 3018–3027. (doi:10.1242/jeb.069005)
- Catmull E, Clark J. 1978 Recursively generated B-spline surfaces on arbitrary topological meshes. *Computer-Aided Des.* **10**, 350–355. (doi:10.1016/0010-4485(78)90110-0)
- Harbig RR, Sheridan J, Thompson MC. 2013 Reynolds number and aspect ratio effects on the leading-edge vortex for rotating insect wing planforms. *J. Fluid Mech.* **717**, 166–192. (doi:10.1017/jfm.2012.565)
- Dong H, Mittal R, Najjar FM. 2006 Wake topology and hydrodynamic performance of low aspect-ratio flapping foils. *J. Fluid Mech.* **556**, 309–343. (doi:10.1017/S002211200600190X)
- Mittal R, Dong H, Bozkurttas M, Najjar FM, Vargas A, von Loebbecke A. 2008 A versatile sharp interface immersed boundary method for incompressible flows with complex boundaries. *J. Comput. Phys.* **227**, 4825–4852. (doi:10.1016/j.jcp.2008.01.028)
- Aono H, Liang F, Liu H. 2008 Near- and far-field aerodynamics in insect hovering flight: an integrated computational study. *J. Exp. Biol.* **211**, 239–257. (doi:10.1242/jeb.008649)

36. Hunt JCR, Wray AA, Moin P. 1988 Eddies, stream, and convergence zones in turbulent flows. See <http://ctr.stanford.edu/Summer/201306111537.pdf>.
37. Fry SN, Sayaman R, Dickinson MH. 2005 The aerodynamics of hovering flight in *Drosophila*. *J. Exp. Biol.* **208**, 2303–2318. (doi:10.1242/jeb.01612)
38. Lehmann FO, Dickinson MH. 1997 The changes in power requirements and muscle efficiency during elevated force production in the fruit fly *Drosophila melanogaster*. *J. Exp. Biol.* **200**, 1133–1143.
39. Sun M, Wu JH. 2003 Aerodynamic force generation and power requirements in forward flight in a fruit fly with modeled wing motion. *J. Exp. Biol.* **206**, 3065–3083. (doi:10.1242/jeb.00517)
40. Aono H, Liu H. 2006 Vortical structure and aerodynamics of hawkmoth hovering. *J. Biomech. Sci. Eng.* **1**, 234–245. (doi:10.1299/jbse.1.234)
41. Song F, Lee KL, Soh AK, Zhu F, Bai YL. 2004 Experimental studies of the material properties of the forewing of cicada (Homoptera, Cicadidae). *J. Exp. Biol.* **207**, 3035–3042. (doi:10.1242/jeb.01122)
42. Bartholomew GA, Barnhart MC. 1984 Tracheal gases, respiratory gas-exchange, body-temperature and flight in some tropical cicadas. *J. Exp. Biol.* **111**, 131–144.
43. Sanborn AF, Heath JE, Heath MS, Noriega FG. 1995 Thermoregulation by endogenous heat-production in 2 south-American grass dwelling cicadas (Homoptera, Cicadidae, Proarna). *Fla Entomol.* **78**, 319–328. (doi:10.2307/3495905)
44. Dickinson MH, Lighton JR. 1995 Muscle efficiency and elastic storage in the flight motor of *Drosophila*. *Science* **268**, 87–90. (doi:10.1126/science.7701346)
45. Vogel S. 2003 *Comparative biomechanics: life's physical world*. Princeton, NJ: Princeton University Press.
46. Dudley R, Ellington CP. 1990 Mechanics of forward flight in bumblebees. 2. Quasi-steady lift and power requirements. *J. Exp. Biol.* **148**, 53–88.
47. Ellington CP. 1984 The aerodynamics of hovering insect flight. VI. Lift and power requirements. *Phil. Trans. R. Soc. Lond. B* **305**, 145–181. (doi:10.1098/rstb.1984.0054)
48. Berman GJ, Wang ZJ. 2007 Energy-minimizing kinematics in hovering insect flight. *J. Fluid Mech.* **582**, 153–168. (doi:10.1017/S0022112007006209)
49. Bomphrey RJ, Taylor GK, Lawson NJ, Thomas ALR. 2006 Digital particle image velocimetry measurements of the downwash distribution of a desert locust *Schistocerca gregaria*. *J. R. Soc. Interface* **3**, 311–317. (doi:10.1098/rsif.2005.0090)